Chemical Science

EDGE ARTICLE

View Article Online
View Journal | View Issue

Cite this: *Chem. Sci.*, 2017, **8**, 2782

Long wavelength excitable near-infrared fluorescent nanoparticles with aggregation-induced emission characteristics for image-guided tumor resection†

Jie Liu,‡[a] Chao Chen,‡[b] Shenglu Ji,[b] Qian Liu,*[c] Dan Ding,*[b] Dan Zhao[a] and Bin Liu*[a]

Received 2nd October 2016
Accepted 20th January 2017

DOI: 10.1039/c6sc04384d

rsc.li/chemical-science

Near infrared (NIR) fluorescence imaging (700–900 nm) is a promising technology in preclinical and clinical tumor diagnosis and therapy. The availability of excellent NIR fluorescent contrast agents is still the main barrier to implementing this technology. Herein, we report the design and synthesis of two series of NIR fluorescent molecules with long wavelength excitation and aggregation-induced emission (AIE) characteristics by fine-tuning their molecular structures and substituents. Further self-assembly between an amphiphilic block co-polymer and the obtained AIE molecules leads to AIE nanoparticles (AIE NPs), which have absorption maxima at 635 nm and emission maxima between 800 and 815 nm with quantum yields of up to 4.8% in aggregated states. *In vitro* and *in vivo* toxicity results demonstrate that the synthesized AIE NPs are biocompatible. Finally, the synthesized AIE NPs have been successfully used for image-guided tumor resection with a high tumor-to-normal tissue signal ratio of 7.2.

Introduction

Near-infrared (NIR, 700–900 nm) fluorescence imaging has been widely employed in preclinical research and clinical practice for noninvasive real-time tumor diagnosis and image-guided cancer surgery.[1–6] This is driven by its unique advantages including deep light penetration (up to centimetre scale), negligible autofluorescence in the NIR spectrum, good safety without ionizing radiation, no requirement for complex infrastructure, and real-time visualization capabilities.[7–10] This technology requires NIR fluorescent agents with superior chemical and photophysical properties. Among the various NIR fluorescent contrast agents investigated to date, organic NIR fluorescent nanoparticles (NPs) have been actively pursued in recent years due to their synthetic versatility and fewer cytotoxicity concerns.[11–15] Moreover, each organic NP can encapsulate a large number of organic dyes,[16] which exhibit better photostability than a single dye molecule. However, the confinement of a large number of organic dyes in a small space often results in weakened or quenched fluorescence due to π–π stacking and/or other nonradiative pathways, known as aggregation-caused quenching (ACQ).[17] In addition, traditional organic dye loaded NPs inherently suffer from small Stokes shifts, which affects the imaging signal collection. These limitations have prevented the advancement of bright and photostable NIR fluorescent organic NPs. Apart from NIR emission (700–900 nm), long wavelength excitation (*e.g.* red or NIR excitation) is also highly desirable for achieving high contrast for *in vivo* imaging applications.

Fluorescent NPs with aggregation-induced emission (AIE NPs) have recently been recognized as a new type of promising fluorescent probe.[18–21] AIE NPs employ molecules with AIE characteristics as fluorescent materials, which exhibit strong fluorescence in the aggregated state, and thus provide a straightforward solution to the ACQ problem faced by conventional organic dyes and inorganic NPs.[22] So far, AIE NPs with blue to NIR emission have been successfully developed and applied to *in vitro* and *in vivo* applications,[23–36] which has revealed that AIE NPs have a higher brightness, larger Stokes shift and stronger photobleaching resistance than conventional organic dyes as well as better biocompatibility compared to quantum dots.[28,30] However, the currently available NIR AIE NPs are not ideal for *in vivo* applications as most of their emission spectra are located below 700 nm with absorption maxima below 500 nm.[28–35,37,38] Although we have previously demonstrated NIR emission in the range of

[a]*Department of Chemical and Biomolecular Engineering, National University of Singapore, 4 Engineering Drive 4, 117585, Singapore. E-mail: cheliub@nus.edu.sg*
[b]*State Key Laboratory of Medicinal Chemical Biology, Key Laboratory of Bioactive Materials, Ministry of Education, College of Life Sciences, Nankai University, Tianjin 300071, P. R. China. E-mail: dingd@nankai.edu.cn*
[c]*Department of Urology, Tianjin First Central Hospital, Tianjin 300192, P. R. China. E-mail: simonlq@163.com*

† Electronic Supplementary Information (ESI) available: Detailed experimental methods, synthesis and characterization of α-DTPEBBTD-C*x* and β-DTPEBBTD-C*x*, cell imaging, *in vitro* and *in vivo* toxicities, biodistribution, blood circulation, and hematoxylin and eosin (H&E) histological analyses. See DOI: 10.1039/c6sc04384d

‡ These authors contributed equally to this work.

700–900 nm with AIE molecules through a Förster resonance energy transfer (FRET) strategy in a blend system,[39] which used an AIE molecule (TPETPAFN) as the donor and a NIR fluorescent dye (NIR775) as the acceptor, the obtained NPs exhibit absorption at 510 nm, showing excitation characteristics of the energy donor and emission properties of the acceptor. Therefore, the development of new AIE NPs with NIR fluorescence, but more importantly, with long wavelength absorption is still challenging.

To obtain NIR fluorescent AIE NPs with red/NIR absorption, the employed molecules should have a narrow bandgap and AIE characteristics. Although attaching AIE-enabling units to ACQ dyes has successfully transformed many of them into AIE ones, limited success has been realized for AIE molecules with both red/NIR absorption and NIR emission.[28] The unsuccessful examples indicate that other factors co-exist to non-radiatively consume the energy in aggregates, which competes with the AIE process. Identifying the underlying factors and finding strategies to eliminate or alleviate the competing process would open up new avenues to design long wavelength excitable and highly emissive NIR AIE molecules in the aggregated state. In this contribution, we report the design and synthesis of two series of NIR fluorescent AIE molecules with long wavelength excitation. We explore how the backbone design could realize long wavelength absorption and emission and how the position and length of the substituted alkoxy chains on the tetraphenylethene (TPE) blocks could affect their AIE features and optical properties. As a proof-of-concept, using α-DTPEBBTD-C4 as a model compound, the formulated AIE NPs have been used to explore their potential applications for intraoperative NIR fluorescence image-guided cancer surgery. Experiments on mouse models with peritoneal carcinomatosis demonstrate that the AIE NPs are effective in guiding the surgeons in the real-time visualization and removal of tumors with a high tumor-to-normal tissue ratio.

Results and discussion

Design, synthesis and characterization of NIR AIE molecules

To fully match the ideal requirements for *in vivo* imaging applications, the emission maximum of AIE NPs in the range of 780–820 nm is preferred to ensure that most of the spectra falls within the NIR window (700–900 nm) for signal collection. To realize this goal, we designed and synthesized two series of donor–acceptor–donor (D–A–D) structured compounds: α-DTPEBBTD-C*x* and β-DTPEBBTD-C*x*, where *x* represents the number of carbon atoms of the alkoxy chain on the TPE blocks, and *x* is 1, 4 or 8 (Scheme 1). The molecular design is based on the following considerations. Benzo[1,2-*c*:4,5-*c*′]bis([1,2,5]thiadiazole) (BBTD) was chosen as an electron acceptor because of its very strong electron-deficient character. It has been readily used to construct D–A structured conjugated polymers or small molecules with various narrow bandgaps for organic optoelectronic devices.[40–43] However, these materials are almost nonfluorescent in the solid state due to strong intramolecular charge transfer and ACQ effects. Herein, we choose monoalkoxy-substituted TPE as a relatively weak electron donor and molecular rotor to form D–A–D structures with BBTD, hoping to yield NIR emissive AIE molecules with desirable absorption and emission maxima for *in vivo* imaging applications. Furthermore, slight structural changes by increasing the side chain length or varying the substituent positions are proposed to adjust the intermolecular interactions (*e.g.*, π–π stacking) for fluorescence enhancement.[44] The detailed synthetic procedures and characterization are available in the ESI (Fig. S1–S17†). It should be noted that β-DTPEBBTD-C*x* consists of isomers due to the geometrical difference in the positions of momoalkoxyphenyl groups, but α-DTPEBBTD-C*x* does not.

The AIE characteristics of α-DTPEBBTD-C*x* and β-DTPEBBTD-C*x* were verified by studying their photoluminescence (PL) spectra in a mixture of THF/water with varying water fractions (f_w), which enabled fine-tuning of the solvent polarity and the extent of solute aggregation. As shown in Fig. 1, all of the compounds exhibit similar PL spectral changes. Generally, they display weak NIR fluorescence in pure THF solution, and their fluorescence intensities are weakened by gradually adding water in THF ($f_w \leq 50$ vol%, except for α-DTPEBBTD-C1, which shows fluorescence enhancement when f_w is >20 vol% due its poor solubility), accompanied with spectral red-shifts, due to their twisted intramolecular charge transfer (TICT) state. The presence of TICT in these molecules was also confirmed by their solvent-dependent emission (ESI Fig. S18†). When the f_w exceeds 50 vol%, the molecules undergo a transition from molecular species to aggregates as evidenced by the laser light scattering (LLS) results (ESI Fig. S19,† taking β-DTPEBBTD-C1 as an example), and the fact that their fluorescence intensities dramatically increase. As shown in Fig. 1, all of the compounds show higher fluorescence intensities in aggregates than in pure THF, indicative of AIE characteristics. Interestingly, the extent of fluorescence enhancement is generally increased with the alkoxy chain length, and α-DTPEBBTD-C*x* shows slightly higher fluorescence than β-DTPEBBTD-C*x* when they have the same side chain length. In addition, when the molecules aggregate, the local environment is less polar than that of water, and gradual blue shifts are observed for the emission maxima when f_w changes from 50 vol% to 90 vol% (from ~836 nm to 798 nm for α-DTPEBBTD-C*x* and to 816 nm for β-DTPEBBTD-C*x*), owing to the TICT-to-local emission transition.[45] These results verify our initial expectation that the designed molecules not only show AIE characteristics but also have emission maxima in the 780–820 nm range.

Fabrication and characterization of AIE NPs

To make the AIE molecules suitable for biological applications, amphiphilic DSPE-PEG_{2000} was employed as the matrix to formulate them into AIE NPs through a nanoprecipitation approach (Fig. 2a). All the AIE NPs show similar sizes and spherical morphologies, as evidenced by transmission electron microscopy (TEM) studies. Fig. 2b shows the representative results for α-DTPEBBTD-C4 based AIE NPs, revealing that the AIE NPs have a spherical shape with a mean diameter of 46 nm, which is slightly smaller than that obtained from laser light scattering (LLS, 54 nm). The obtained AIE NPs can be stored at

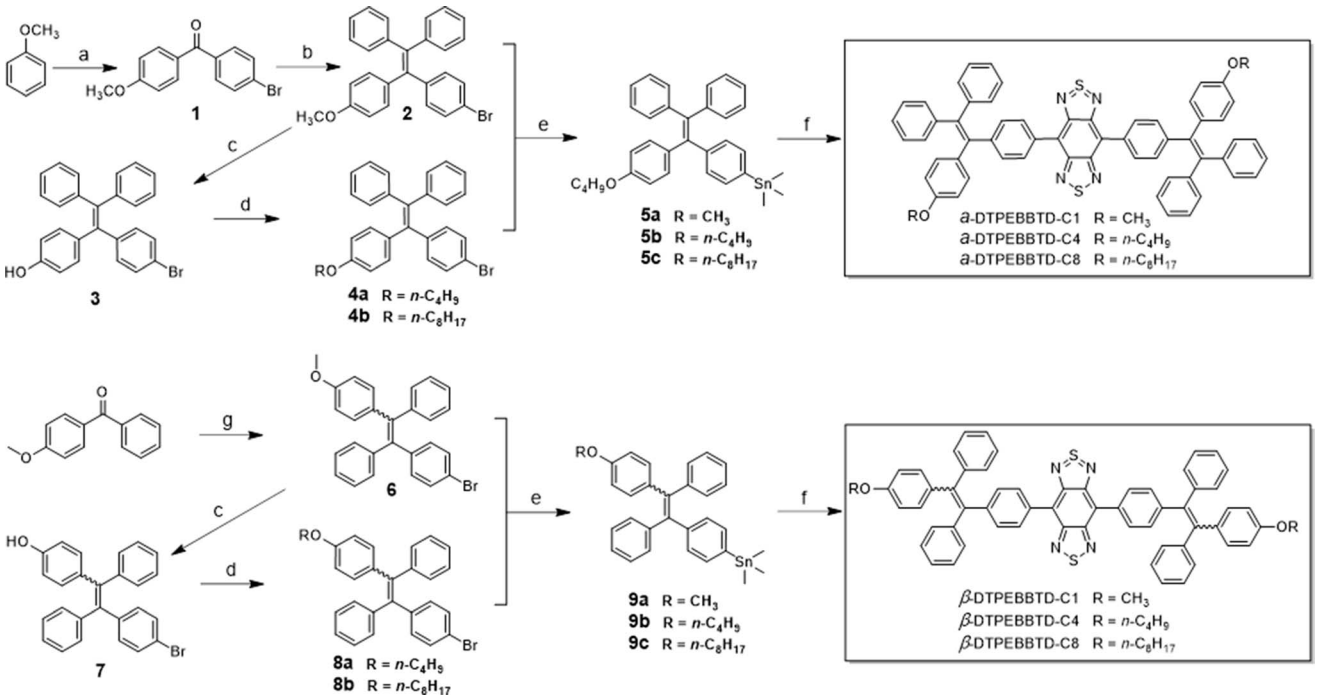

Scheme 1 Chemical structures and synthetic routes to α-DTPEBBTD-C*x* and β-DTPEBBTD-C*x*. *x* represents the carbon numbers of the alkoxy chains on the TPE blocks, and $x = 1$, 4 or 8. Reagents and conditions: (a) $AlCl_3$, 4-bromobenzoyl chloride, CH_2Cl_2, 0–10 °C, overnight; (b) (i) BuLi, diphenylmethane, 0 °C, overnight; (ii) *p*-toluenesulfonic acid, toluene, 100 °C, 3 h; (c) BBr_3, CH_2Cl_2; (d) Cs_2CO_3, DMF, room temperature, 1-bromobutane for 4a and 8a, 1-bromooctane for 4b and 8b; (e) BuLi, Me_3SnCl, THF, −78 °C, overnight; (f) $Pd(PPh_3)_4$, toluene, 100 °C, 24 h.

4 °C for over 3 months without any precipitation, indicating their good colloidal stability. The absorption spectra of α-DTPEBBTD-C*x* and β-DTPEBBTD-C*x* based AIE NPs are shown in Fig. 2c. The absorption bands from 300 to 450 nm are assigned to the π–π* and n–π* transitions of the conjugated aromatic skeleton while the lower energy bands peaked at ~635 nm are attributed to the ICT from the donor TPE to acceptor BBTD. Distinct from all the existing AIE NPs, the absorption maxima of both series are located in the 500–750 nm range, and the peak wavelength of ~635 nm perfectly matches

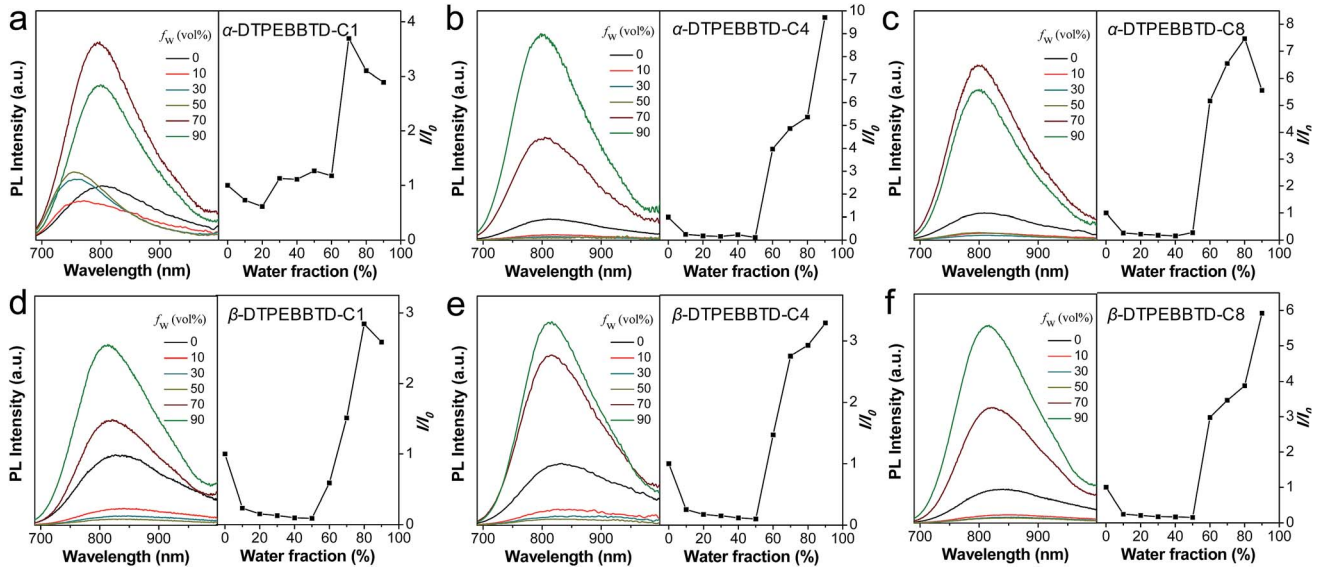

Fig. 1 Study of aggregation-induced emission. PL spectra and plots of the relative PL intensity of α-DTPEBBTD-C*x* and β-DTPEBBTD-C*x* in THF/H_2O mixtures with different volume fractions of water (f_w). I_0 and I are the PL intensities of α-DTPEBBTD-C*x* and β-DTPEBBTD-C*x* in pure THF ($f_w = 0$) and THF/water mixtures with specific f_ws, respectively. $\lambda_{ex} = 635$ nm. The concentration is 5 μM.

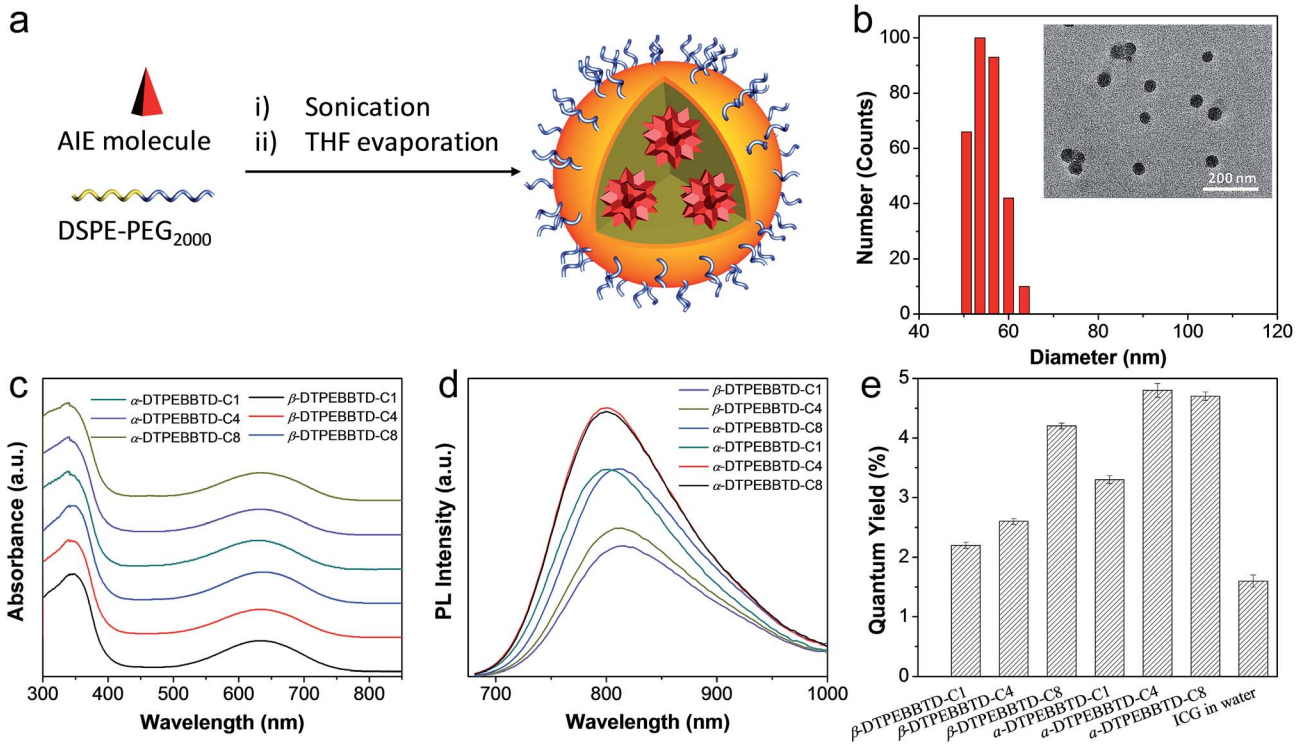

Fig. 2 Preparation and characterization of the AIE NPs. (a) Schematic illustration of AIE NP preparation. (b) Representative LLS and TEM results of α-DTPEBBTD-C4 based AIE NPs. (c) UV-vis absorption and (d) PL spectra of the AIE NPs in water. (e) Quantum yields of the AIE NPs and ICG in water.

the commercially available 635 nm laser line, which ensures the most efficient utilization of their light-harvesting ability. The absorption spectra are almost identical for all of the molecules, indicating that the variation of position and length of the substituents has little effect on their ground states, which is also supported by the constant HOMO and LUMO levels (ESI Fig. S20†). As shown in Fig. 2d, the emission spectra of all of the AIE NPs are mainly located within the 700–900 nm region, which is beneficial to *in vivo* NIR fluorescence imaging. Unlike the similar absorption profiles, the PL spectra of the AIE NPs show three general trends. Firstly, the fluorescence intensity is gradually enhanced with the side chain length, due to their perturbation of the intermolecular interactions. Secondly, as compared to β-DTPEBBTD-C*x* based AIE NPs, α-DTPEBBTD-C*x* based NPs show blue-shifted emission maxima (~801 nm *versus* ~815 nm) and slightly smaller Stokes shifts (136 nm *versus* 150 nm). This is because the alkoxy on the β-phenyl has better electronic communication along the conjugated skeleton as compared to that on the α-phenyl. The overall large Stokes shifts of the AIE NPs should greatly minimize the self-absorption effect typically observed in conventional NIR dyes. Thirdly, α-DTPEBBTD-C*x* based AIE NPs have a stronger fluorescence than β-DTPEBBTD-C*x* based ones, presumably because of the ordered β-DTPEBBTD-C*x* structures, which favour better molecular packing than the α-DTPEBBTD-C*x* series in the aggregated state. As demonstrated by the X-ray diffraction (XRD) patterns (ESI, Fig. S21†), taking α-DTPEBBTD-C1 and β-DTPEBBTD-C1 as examples, solid α-DTPEBBTD-C1 is mainly in the amorphous state, while β-DTPEBBTD-C1 still shows some small crystal peaks, indicative of better molecular packing for β-DTPEBBTD-C1.

The effect of substitution on their optical properties is also reflected in their quantum yields (QYs), which were determined using IR-125 in DMSO as a reference (QY = 13%).[46] Fig. 2e shows that the QY of the AIE NPs is gradually increased when longer substituents are used (from 3.8% to 4.8% for α-DTPEBBTD-C*x* and from 2.2% to 3.8% for β-DTPEBBTD-C*x* based AIE NPs). The AIE NPs also show higher QY than indocyanine green (ICG, QY = 1.6%) in water. ICG was chosen as a reference for comparison, because it is a NIR fluorescent dye approved for clinical use by the Food and Drug administration (FDA), which has been widely used for medical diagnostics and image-guided surgery. The intense NIR fluorescence observed for the AIE NPs can be attributed to the AIE effect caused by the aggregates' formation, which restricts the intramolecular motions.[20] In addition, the presence of substituted side chains on the TPE blocks also works together to enhance the fluorescence intensity. In the following *in vitro* and *in vivo* experiments, α-DTPEBBTD-C4 based AIE NPs were used by virtue of their highest QY and well-defined chemical structure.

Comparison between α-DTPEBBTD-C4 based AIE NPs and ICG

For *in vivo* imaging, it is necessary to assess the brightness, photo and thermal stabilities of the contrast agent. Integration of the emission spectrum between 700–900 nm reveals that AIE

NPs show a linear brightness increase with concentration while ICG exhibits an increase first (0–4 μM) followed by a decrease at higher concentrations (Fig. 3a), suggesting that AIE NPs do not suffer from the ACQ problem faced by ICG. The thermal stabilities of AIE NPs and ICG were evaluated by incubating them in phosphate-buffered saline (PBS) at 37 °C for 7 days. As shown in Fig. 3b, AIE NPs remain almost constant in their fluorescence intensities, while ICG shows a ~75% fluorescence intensity loss after 7 days under the same conditions, suggesting that AIE NPs have better thermal stability. Once both the AIE NPs and ICG are exposed to white light (0.25 W cm^{-2}) for 10 min, the fluorescence intensities decrease by ~15% for AIE NPs and by ~86% for ICG (Fig. 3c), indicative of the better photostability of the AIE NPs.

Evaluation of cellular imaging, biocompatibility and metabolization of AIE NPs

The capacity of α-DTPEBBTD-C4 based AIE NPs in cellular imaging was evaluated by confocal laser scanning microscopy (CLSM) using 4T1 breast cancer cells as an example. The 3D confocal image obtained upon excitation at 633 nm gives a high-contrast signal due to its high NIR fluorescence (ESI Fig. S22†). The cellular toxicity of α-DTPEBBTD-C4 based AIE NPs against 4T1 cancer cells and L02 hepatic cells (normal cells) was studied using 3-(4,5-dimethylthiazol-2-yl)-2,5-diphenyl tetrazolium bromide (MTT) assays, revealing their low cytotoxicity after 48 h incubation (ESI Fig. S23†). *In vivo* toxicity of the AIE NPs was also evaluated by intravenous injection of the AIE NPs into healthy mice, in which the NP concentration for assessment of *in vivo* toxicity (100 nM) is two-times higher than that used for the following image-guided surgery experiments. The data including mouse body weight changes over time and the blood chemistry tests on day 9 post AIE NP administration indicate that the α-DTPEBBTD-C4 based AIE NPs have no observable *in vivo* toxicity (ESI Fig. S24–S26†). The studies on biodistribution and metabolization of AIE NPs in mice were also performed, and the results are displayed in the ESI Fig. S27.† After intravenous injection of the AIE NPs (50 nM), strong fluorescence signals are observed in the liver and spleen within the initial several hours post-injection because of the AIE NP uptake by the well-known reticuloendothelial system (RES).[47] The fluorescence intensities in RES organs significantly decrease at 48 h and almost vanish on day 10 post-injection, suggesting that AIE NPs will not stay in the body for a long period of time. Additionally, obvious NIR fluorescence is observed in the collected feces of AIE-NP-administrated mice, implying that the excretion of AIE-NPs is mainly *via* the biliary pathway.[48] It is noteworthy that, throughout the 10 day monitoring, nearly no fluorescence signals were detected in other tissues including heart, lung, intestine, stomach, kidney, brain, muscle and skin, proving the safety of AIE NPs for *in vivo* applications. Moreover, the half-life of AIE NPs in blood circulation is calculated to be around 1.8 h (ESI Fig. S28†), which is similar to that of PEG-coated nanomaterials.[49,50]

AIE NPs for tumor diagnosis

The promising results above motivated us to use the bright AIE NPs as a fluorescent contrast agent for tumor identification and image-guided tumor resection, as image-guided cancer surgery using NIR fluorescence has emerged as an advanced strategy in clinical cancer therapy.[6,51,52] Before the AIE NPs were used for image-guided tumor resection, it is necessary to evaluate their capability in intraoperative tumor identification. To this end, a peritoneal carcinomatosis-bearing mouse model was established by intraperitoneal inoculation of luciferase-expressed 4T1 tumor cells, which led to the formation of small tumor nodules scattered in the peritoneal cavity, especially on the surface of the intestines. It is well known that the *in vivo* distribution of tumor nodules can be precisely reported by bioluminescence from luciferase upon injection of D-luciferin, the substrate of luciferase, into the mice.[53] The AIE NPs were intravenously injected into the peritoneal carcinomatosis-bearing mice. At 24 h post-injection, the mouse abdomen was opened, followed by simultaneous bioluminescence and fluorescence imaging. As shown in Fig. 4a, the bioluminescence imaging study reveals that many tumor nodules are located within the mouse peritoneal cavity. On the other hand, Fig. 4b shows the *in vivo* fluorescence image of the same region of AIE

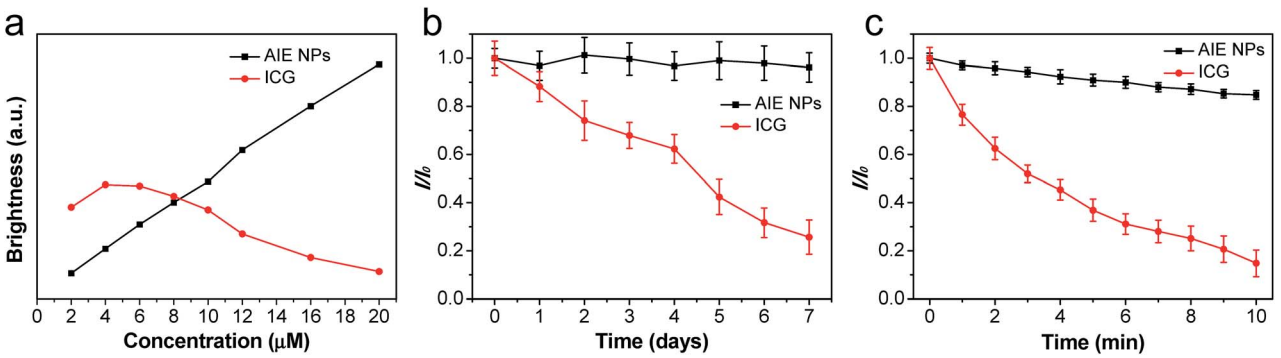

Fig. 3 Comparison between α-DTPEBBTD-C4 based AIE NPs and ICG. (a) Brightness of AIE NPs and ICG at different concentrations. (b) Fluorescence intensity changes of AIE NPs and ICG upon incubation in PBS buffer at 37 °C for 7 days. (c) Fluorescence intensity changes of AIE NPs and ICG upon irradiation with white light for 10 min. I_0 and I in both (b) and (c) represent the initial and specific time point fluorescence intensities, respectively.

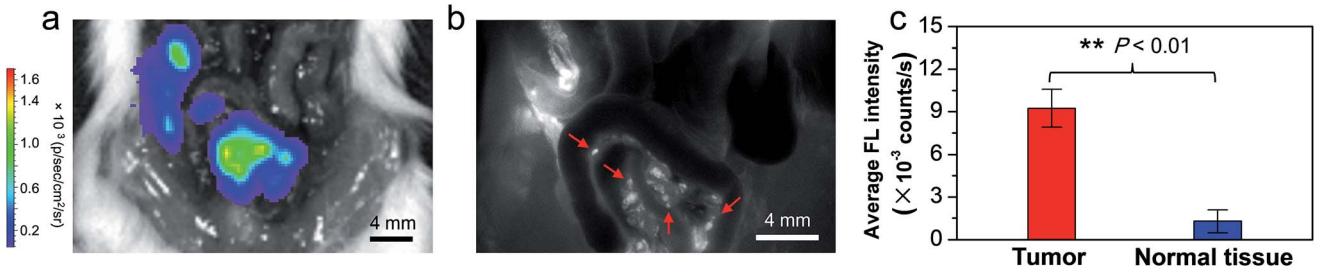

Fig. 4 α-DTPEBBTD-C4 based AIE NPs for tumor identification. (a) Bioluminescence, and (b) fluorescence images of peritoneal carcinomatosis-bearing mice after intravenous injection of α-DTPEBBTD-C4 based AIE NPs for 24 h. The red arrows indicate the submillimeter tumors in the peritoneal cavity. (c) The average fluorescence intensity of tumors and surrounding normal tissues from α-DTPEBBTD-C4 based AIE NP treated mice. The error bars were based on results from 5 mice.

NP-injected mice as that in Fig. 4a. Encouragingly, the AIE NPs show a prominent enhanced permeability and retention (EPR) effect and the bright NIR fluorescence can distinctly delineate tumor nodules over normal tissues (Fig. 4b). The excellent overlap between the bioluminescence and fluorescence patterns at the tumor sites suggests the high accuracy of AIE NPs in tumor detection.

To further confirm that the bright fluorescence in the tumor nodules is indeed originated from the AIE NPs, the spectral unmixing function of the Maestro software package was employed to separate the pure signal and mouse autofluorescence. As shown in the ESI Fig. S29,† the resultant fluorescence spectrum is similar to that of the AIE NPs in aqueous solution recorded by a fluorescence spectrometer, validating that the fluorescence is indeed from the AIE NPs. It is also found that the average fluorescence intensity from the tumor nodules is statistically higher than that from the surrounding normal tissues ($P < 0.01$; Fig. 4c), yielding a tumor-to-normal tissue (T/NT) ratio of ~7.2, which surpasses the Rose criterion of 5.[54] This ratio is significantly higher than those for the currently reported NIR fluorescent probes, such as ICG and methylene blue (MB) (T/NT < 5) in image-guided surgery.[2,55] Furthermore, the tumor margins toward adjacent tissues can be explicitly determined by the AIE NP fluorescence in both the excised intestine and peritoneum, which were further confirmed by hematoxylin and eosin (H&E) histological analyses (ESI Fig. S30†). In addition,

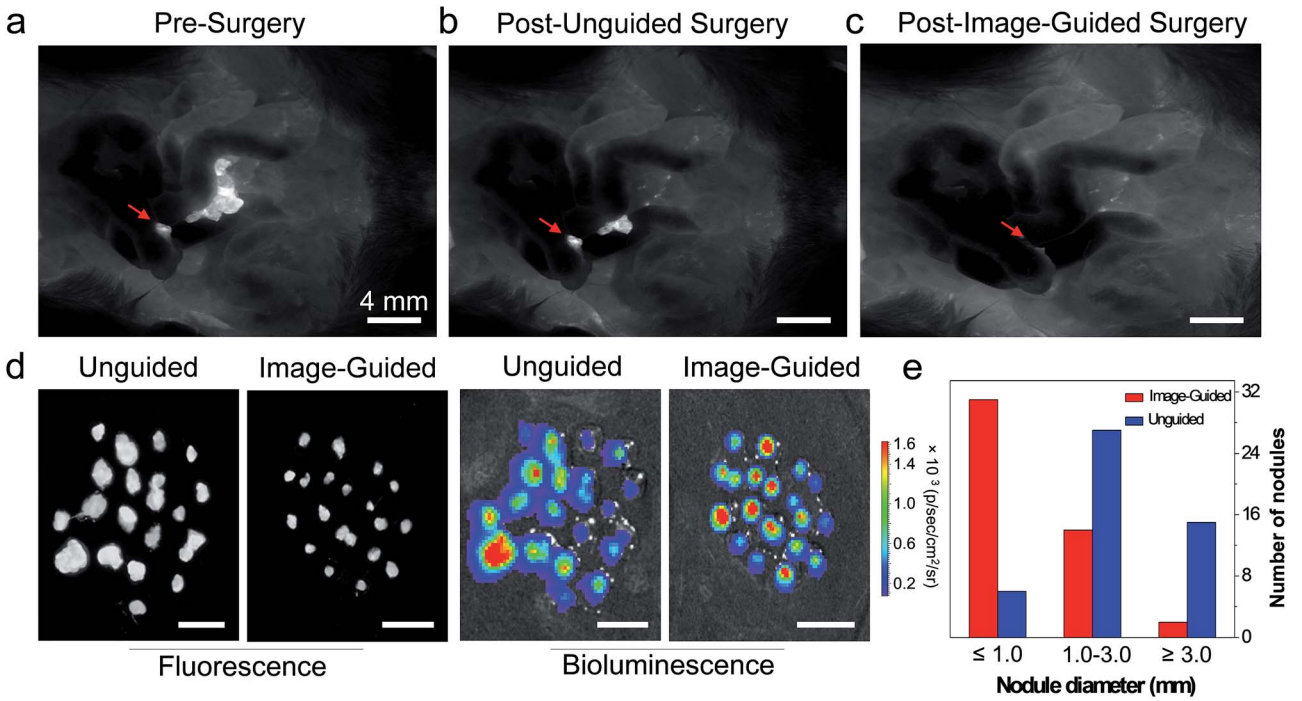

Fig. 5 Tumor resection with and without AIE NP image-guided surgery. Representative fluorescence images (a) before operation, (b) after operation under white light, and (c) after re-operation with the aid of AIE NP image-guidance. Red arrows in (a–c) indicate the location of a tiny nodule only detectable during image-guided surgery. (d) The extracted nodules from unguided groups and AIE NP guided groups were examined with a fluorescence imaging system (left) and a bioluminescence imaging system (right). (e) Histogram of nodule diameters extracted from unguided and AIE NP-guided groups.

a mouse model with lung metastasis of carcinoma was also set up to evaluate the ability of AIE NPs in identification of pulmonary nodules. As displayed in the ESI Fig. S31a,† although a number of big tumor nodules in the lung tissue are visible to the naked eye under white light, the NIR fluorescence guidance *via* intravenously injected AIE NPs provides momentous information on the location of very tiny tumors with sizes of less than 500 μm. These tiny tumors are verified by H&E-staining analysis to have diameters of 100–500 μm. Besides pulmonary nodules, the tumor metastasis to the heart can also be visualized by AIE NPs (ESI Fig. S31b†). These results collectively manifest that the AIE NPs are effective in the real-time identification of tumors (especially submillimeter tumors) with high-contrast between tumors and normal tissues.

Image-guided tumor resection using AIE NPs as a fluorescent contrast agent

To investigate the practical application of AIE NPs in image-guided tumor resection, mice with peritoneal carcinomatosis were injected with AIE NPs *via* their tail veins. Before operation, the mice were observed under a fluorescence imaging system and lots of tumors could be clearly distinguished with a high signal-to-noise ratio (Fig. 5a). Then a surgeon who was blinded to the fluorescence imaging performed the surgery with his experience. As shown in Fig. 5b, the tumor nodules, especially those below 1 mm in diameter could not be harvested completely by the surgeon without the guidance of AIE NP fluorescence. After a second resection with the aid of AIE NP-guided fluorescence imaging, nearly all of the tumor nodules were removed (Fig. 5c). The extracted nodules from unguided groups and AIE NP guided groups were examined with fluorescence imaging and bioluminescence imaging systems. As shown in Fig. 5d, the fluorescence and bioluminescence signals from resected tumor nodules overlap very well, indicating that the surgery did not lead to any unnecessary resection of healthy tissues, thanks to the accurate tumor identification ability of AIE NPs. Importantly, on average, 98% more tumor nodules were removed with the guidance of AIE NP fluorescence compared to unguided groups (Fig. 5e). The noteworthy advantage of using NIR fluorescence guidance is that additional small nodules (less than 500 μm in diameter) were excised, and that they were otherwise undetectable without NIR fluorescence guidance (31 *versus* 6 nodules). These results demonstrate that NIR fluorescent AIE NPs are able to facilitate accurate tumor determination and resection during surgery.

Conclusions

In summary, we report the first long wavelength excitable NIR fluorescent AIE NPs with bright emission for image-guided cancer surgery. The absorption and emission profiles of the AIE NPs were manipulated to match the *in vivo* fluorescence imaging system through the systematic study of the position and length of the alkoxy chains. The present study shows that the incorporation of alkoxy substitutions into TPE blocks does not have any obvious effect on the bandgap of the obtained molecules, but indeed imparts the obtained α- and β-DTPEBBTD-C*x* with AIE features. This finding indicates that reducing the intermolecular interaction plays an important role in alleviating the undesirable processes for realization of AIE features. Moreover, due to the advantages of high brightness, excellent biocompatibility, and a prominent EPR effect, the obtained NIR fluorescent α-DTPEBBTD-C4 NPs have been successfully applied to NIR fluorescence image-guided cancer surgery. They have demonstrated great potential in high accuracy tumor detection with a high tumor-to-normal tissue ratio of 7.2, which enabled the surgeons to perform image-guided surgery to remove tiny tumors. Additionally, as compared to clinically available NIR fluorescent agents, such as ICG and MB, the AIE NPs have overcome their inherent drawbacks such as small Stokes shift, poor photostability and low fluorescence in the aggregated state. As compared to the previously reported NIR AIE NPs, the AIE NPs present in this work simultaneously have long wavelength excitation and NIR emission (700–900 nm), which are more desirable for *in vivo* imaging and image-guided surgery. With the further advancement of AIE molecules, we believe that AIE NPs could afford more sensitive and accurate guidance of cancer resection to potentially achieve better surgical outcomes in the near future.

Acknowledgements

The authors are grateful to the Singapore National Research Foundation (R279-000-444-281 and R279-000-483-281), National University of Singapore (R279-000-482-133), Singapore Ministry of Education (AcRF Tier 2 R-279-000-429-112) and the National Natural Science Foundation of China (81301311 and 31571011) for financial support.

Notes and references

1 H. S. Choi, S. L. Gibbs, J. H. Lee, S. H. Kim, Y. Ashitate, F. B. Liu, H. Hyun, G. Park, Y. Xie, S. Bae, M. Henary and J. V. Frangioni, *Nat. Biotechnol.*, 2013, **31**, 148.
2 C. T. Zeng, W. T. Shang, K. Wang, C. W. Chi, X. H. Jia, C. Fang, D. Yang, J. Z. Ye, C. H. Fang and J. Tian, *Sci. Rep.*, 2016, **6**, 21959.
3 B. E. Schaafsma, J. S. D. Mieog, M. Hutteman, J. R. Van der Vorst, P. J. K. Kuppen, C. Lowik, J. V. Frangioni, C. J. H. Van de Velde and A. L. Vahrmeijer, *J. Surg. Oncol.*, 2011, **104**, 323.
4 H. J. M. Handgraaf, F. P. R. Verbeek, Q. R. G. Tummers, L. S. F. Boogerd, C. J. H. van de Velde, A. L. Vahrmeijer and K. N. Gaarenstroom, *Gynecol. Oncol.*, 2014, **135**, 606.
5 R. M. Schols, N. J. Connell and L. P. S. Stassen, *World J. Surg.*, 2015, **39**, 1069.
6 A. L. Vahrmeijer, M. Hutteman, J. R. van der Vorst, C. J. H. van de Velde and J. V. Frangioni, *Nat. Rev. Clin. Oncol.*, 2013, **10**, 507.
7 R. Weissleder, *Nat. Biotechnol.*, 2001, **19**, 316.
8 E. M. Sevick-Muraca, J. P. Houston and M. Gurfinkel, *Curr. Opin. Chem. Biol.*, 2002, **6**, 642.

9 V. Ntziachristos, C. Bremer and R. Weissleder, *Eur. J. Radiol.*, 2003, **13**, 195.
10 S. L. Luo, E. L. Zhang, Y. P. Su, T. M. Cheng and C. M. Shi, *Biomaterials*, 2011, **32**, 7127.
11 X. X. He, K. M. Wang and Z. Cheng, *Wiley Interdiscip. Rev.: Nanomed. Nanobiotechnol.*, 2010, **2**, 349.
12 L. Larush and S. Magdassi, *Nanomedicine*, 2011, **6**, 233.
13 S. A. Hilderbrand and R. Weissleder, *Curr. Opin. Chem. Biol.*, 2010, **14**, 71.
14 P. P. Ghoroghchian, P. R. Frail, K. Susumu, D. Blessington, A. K. Brannan, F. S. Bates, B. Chance, D. A. Hammer and M. J. Therien, *Proc. Natl. Acad. Sci. U. S. A.*, 2005, **102**, 2922.
15 E. I. Altınoğlu, T. J. Russin, J. M. Kaiser, B. M. Barth, P. C. Eklund, M. Kester and J. H. Adair, *ACS Nano*, 2008, **2**, 2075.
16 S. Santra, D. Dutta, G. A. Walter and B. M. Moudgil, *Technol. Cancer Res. Treat.*, 2005, **4**, 593.
17 J. B. Birks, *Photophysics of Aromatic Molecules*, Wiley, London, 1970.
18 J. Mei, Y. N. Hong, J. W. Y. Lam, A. J. Qin, Y. H. Tang and B. Z. Tang, *Adv. Mater.*, 2014, **26**, 5429.
19 J. Mei, N. L. C. Leung, R. T. K. Kwok, J. W. Y. Lam and B. Z. Tang, *Chem. Rev.*, 2015, **115**, 11718.
20 D. Ding, K. Li, B. Liu and B. Z. Tang, *Acc. Chem. Res.*, 2013, **46**, 2441.
21 K. Li and B. Liu, *Chem. Soc. Rev.*, 2014, **43**, 6570.
22 Z. Zhelev, H. Ohba and R. Bakalova, *J. Am. Chem. Soc.*, 2006, **128**, 6324.
23 G. Feng, C. Y. Tay, Q. X. Chui, R. Liu, N. Tomczak, J. Liu, B. Z. Tang, D. T. Leong and B. Liu, *Biomaterials*, 2014, **35**, 8669.
24 X. Cai, A. Bandla, D. Mao, G. Feng, W. Qin, L. D. Liao, N. Thakor, B. Z. Tang and B. Liu, *Adv. Mater.*, 2016, **28**, 8760.
25 X. Cai, C. J. Zhang, F. Ting Wei Lim, S. J. Chan, A. Bandla, C. K. Chuan, F. Hu, S. Xu, N. V. Thakor and L. D. Liao, *Small*, 2016, **12**, 6576.
26 D. Ding, D. Mao, K. Li, X. Wang, W. Qin, R. Liu, D. S. Chiam, N. Tomczak, Z. Yang and B. Z. Tang, *ACS Nano*, 2014, **8**, 12620.
27 Y. Yu, C. Feng, Y. Hong, J. Liu, S. Chen, K. M. Ng, K. Q. Luo and B. Z. Tang, *Adv. Mater.*, 2011, **23**, 3298.
28 W. Qin, D. Ding, J. Liu, W. Z. Yuan, Y. Hu, B. Liu and B. Z. Tang, *Adv. Funct. Mater.*, 2012, **22**, 771.
29 Q. Zhao, K. Li, S. Chen, A. Qin, D. Ding, S. Zhang, Y. Liu, B. Liu, J. Z. Sun and B. Z. Tang, *J. Mater. Chem.*, 2012, **22**, 15128.
30 K. Li, W. Qin, D. Ding, N. Tomczak, J. Geng, R. Liu, J. Liu, X. Zhang, H. Liu and B. Liu, *Sci. Rep.*, 2013, **3**, 1150.
31 D. Ding, K. Li, W. Qin, R. Zhan, Y. Hu, J. Liu, B. Z. Tang and B. Liu, *Adv. Healthcare Mater.*, 2013, **2**, 500.
32 J. Zhang, C. Li, X. Zhang, S. Huo, S. Jin, F.-F. An, X. Wang, X. Xue, C. Okeke and G. Duan, *Biomaterials*, 2015, **42**, 103.
33 J. Zhang, R. Chen, Z. Zhu, C. Adachi, X. Zhang and C.-S. Lee, *ACS Appl. Mater. Interfaces*, 2015, **7**, 26266.
34 Y. Gao, G. Feng, T. Jiang, C. Goh, L. Ng, B. Liu, B. Li, L. Yang, J. Hua and H. Tian, *Adv. Funct. Mater.*, 2015, **25**, 2857.
35 H. Lu, Y. Zheng, X. Zhao, L. Wang, S. Ma, X. Han, B. Xu, W. Tian and H. Gao, *Angew. Chem., Int. Ed.*, 2016, **55**, 155.
36 D. Wang, J. Qian, S. L. He, J. S. Park, K. S. Lee, S. H. Han and Y. Mu, *Biomaterials*, 2011, **32**, 5880.
37 Z. Wang, L. Yan, L. Zhang, Y. Chen, H. Li, J. Zhang, Y. Zhang, X. Li, B. Xu and X. Fu, *Polym. Chem.*, 2014, **5**, 7013.
38 W. Qin, K. Li, G. Feng, M. Li, Z. Yang, B. Liu and B. Z. Tang, *Adv. Funct. Mater.*, 2014, **24**, 635.
39 J. Geng, Z. Zhu, W. Qin, L. Ma, Y. Hu, G. G. Gurzadyan, B. Z. Tang and B. Liu, *Nanoscale*, 2014, **6**, 939.
40 G. Qian, B. Dai, M. Luo, D. Yu, J. Zhan, Z. Zhang, D. Ma and Z. Y. Wang, *Chem. Mater.*, 2008, **20**, 6208.
41 C. Qin, Y. Fu, C. H. Chui, C. W. Kan, Z. Xie, L. Wang and W. Y. Wong, *Macromol. Rapid Commun.*, 2011, **32**, 1472.
42 A. L. Antaris, H. Chen, K. Cheng, Y. Sun, G. Hong, C. Qu, S. Diao, Z. Deng, X. Hu, B. Zhang, X. Zhang, O. K. Yaghi, Z. R. Alamparambil, X. Hong, Z. Cheng and H. Dai, *Nat. Mater.*, 2016, **15**, 235.
43 X. Du, J. Qi, Z. Zhang, D. Ma and Z. Y. Wang, *Chem. Mater.*, 2012, **24**, 2178.
44 T. Ozdemir, S. Atilgan, I. Kutuk, L. T. Yildirim, A. Tulek, M. Bayindir and E. U. Akkaya, *Org. Lett.*, 2009, **11**, 2105.
45 R. Hu, E. Lager, A. Aguilar-Aguilar, J. Liu, J. W. Lam, H. H. Sung, I. D. Williams, Y. Zhong, K. S. Wong and E. Pena-Cabrera, *J. Phys. Chem. C*, 2009, **113**, 15845.
46 R. C. Benson and H. A. Kues, *J. Chem. Eng. Data*, 1977, **22**, 379.
47 O. C. Farokhzad and R. Langer, *ACS Nano*, 2009, **3**, 16.
48 Z. Liu, C. Davis, W. Cai, L. He, X. Chen and H. Dai, *Proc. Natl. Acad. Sci. U. S. A.*, 2008, **105**, 1410.
49 D. Ding, J. Liu, G. Feng, K. Li, Y. Hu and B. Liu, *Small*, 2013, **9**, 3093.
50 K. Yang, S. Zhang, G. Zhang, X. Sun, S.-T. Lee and Z. Liu, *Nano Lett.*, 2010, **10**, 3318.
51 I. Atallah, C. Milet, J. L. Coll, E. Reyt, C. A. Righini and A. Hurbin, *Arch. Oto-Rhino-Laryngol.*, 2015, **272**, 2593.
52 T. Namikawa, T. Sato and K. Hanazaki, *Surg. Today*, 2015, **45**, 1467.
53 H. M. Buchhorn, C. Seidl, R. Beck, D. Saur, C. Apostolidis, A. Morgenstern, M. Schwaiger and R. Senekowitsch-Schmidtke, *Eur. J. Nucl. Med. Mol. Imaging*, 2007, **34**, 841.
54 J. T. Bushberg and J. M. Boone, *The essential physics of medical imaging*, Lippincott Williams &Wilkins, 2011.
55 O. T. Okusanya, D. Holt, D. Heitjan, C. Deshpande, O. Venegas, J. Jiang, R. Judy, E. DeJesus, B. Madajewski and K. Oh, *Ann. Thorac. Surg.*, 2014, **98**, 1223.